IOPscience iopscience.iop.org

Home Search Collections Journals About Contact us My IOPscience

MEMS resonant load cells for micro-mechanical test frames: feasibility study and optimal design

This article has been downloaded from IOPscience. Please scroll down to see the full text article.

2010 J. Micromech. Microeng. 20 125004

(http://iopscience.iop.org/0960-1317/20/12/125004)

View the table of contents for this issue, or go to the journal homepage for more

Download details:
IP Address: 144.122.166.50
The article was downloaded on 18/01/2011 at 16:11

Please note that terms and conditions apply.

J. Micromech. Microeng. **20** (2010) 125004 (17pp) doi:10.1088/0960-1317/20/12/125004

MEMS resonant load cells for micro-mechanical test frames: feasibility study and optimal design

A Torrents[1], K Azgin[1], S W Godfrey[1], E S Topalli[2], T Akin[2] and L Valdevit[1]

[1] Mechanical and Aerospace Engineering Department, University of California, Irvine, CA 92697, USA
[2] Electrical and Electronics Engineering Department and METU-MEMS Center, Middle East Technical University, TR06531, Ankara, Turkey

E-mail: valdevit@uci.edu

Received 2 July 2010, in final form 22 September 2010
Published 8 November 2010
Online at stacks.iop.org/JMM/20/125004

Abstract

This paper presents the design, optimization and manufacturing of a novel micro-fabricated load cell based on a double-ended tuning fork. The device geometry and operating voltages are optimized for maximum force resolution and range, subject to a number of manufacturing and electromechanical constraints. All optimizations are enabled by analytical modeling (verified by selected finite elements analyses) coupled with an efficient C++ code based on the particle swarm optimization algorithm. This assessment indicates that force resolutions of ∼0.5–10 nN are feasible in vacuum (∼1–50 mTorr), with force ranges as large as 1 N. Importantly, the optimal design for vacuum operation is independent of the desired range, ensuring versatility. Experimental verifications on a sub-optimal device fabricated using silicon-on-glass technology demonstrate a resolution of ∼23 nN at a vacuum level of ∼50 mTorr. The device demonstrated in this article will be integrated in a hybrid micro-mechanical test frame for unprecedented combinations of force resolution and range, displacement resolution and range, optical (or SEM) access to the sample, versatility and cost.

(Some figures in this article are in colour only in the electronic version)

1. Introduction

Motivated by the evolution of the micro-electronics and MEMS industries, a staggering number of different techniques have been developed over the last two decades to measure the mechanical properties of materials at a small scale: many of them are reviewed in the excellent articles by Haque and Saif [1] and Bell *et al* [2]. The scale-dependent strengthening effects revealed by these techniques (e.g., in carbon nanotubes [3] and metallic nano-pillars [4]) and the recent progress in advanced manufacturing (e.g., stereolithography [5, 6], manufacturing of 3D micro-trusses by self-propagating polymer waveguides [7]), suggest an incredible opportunity to design and manufacture novel structural materials at a macroscopic scale while retaining accurate dimensional control of micro and nano-scale architectures, with potentially transformative impact on a number of properties and combinations thereof. This vision requires novel testing capabilities. As the unit cells of micro-architected materials can take many shapes and sizes and several base materials can be used, the ideal device should have the following features: (i) be adaptable to samples of vastly different sizes and shapes; (ii) allow controlled displacement actuation and independent load measurement; (iii) be capable of extreme force resolution (∼1–100 nN) and range (∼1 N), displacement resolution (∼10–100 nm) and range (1–10 mm) and (iv) allow optical (or SEM) access to the test coupon with potential for strain mapping (via digital image correlation). To the best of our knowledge, the only devices with all these features are custom-built nanoindenters, coupled with electron microscopes (SEM). Force and displacement resolutions of 50 nN and 0.01 nm, respectively, and ranges of 10 N and 1 mm are readily achievable. Custom-built grips can enable tensile loading. An excellent example of such an instrument is

 © 2010 IOP Publishing Ltd Printed in the UK & the USA

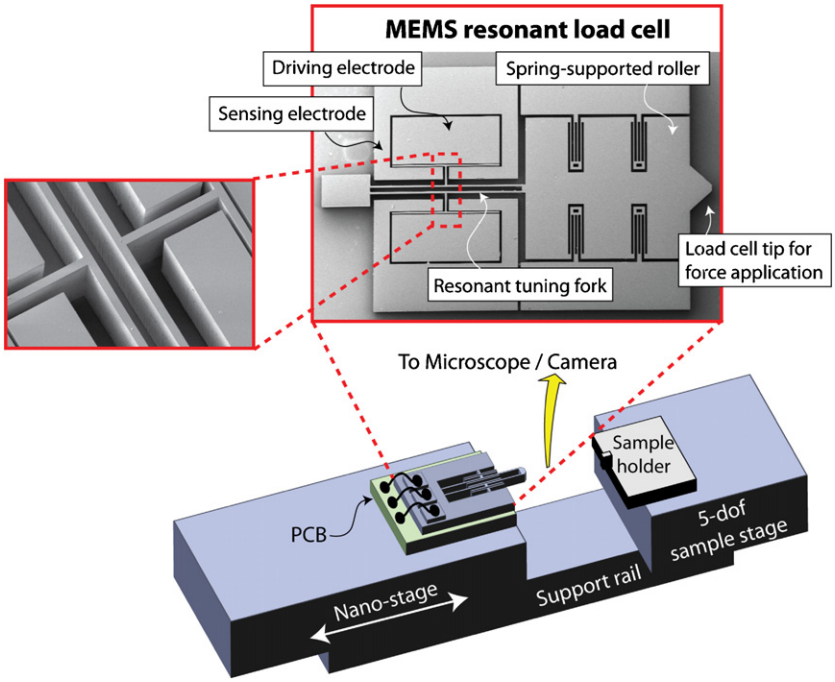


Figure 1. Schematic of the proposed micro-mechanical test frame (μ-MTF). The displacement actuator is a commercially available nano-stage, while the load cell (inset) is microfabricated. The configuration allows for optical access to the sample (with potential for strain mapping). Alignment of the μ-MTF with the sample is achieved through a 5 degree-of-freedom sample holder. The entire system can be inserted in a vacuum chamber, imaging through a window with a long working-distance lens.

described in [8]. In spite of their performance and versatility, these custom units are exceptionally expensive and not readily available to most researchers.

MEMS technology offers a lower cost alternative. A large variety of on-chip MEMS test frames (i.e. devices that include sensor, actuator and often sample on the same chip) are available in the literature. Actuation is generally performed electrostatically [9, 10] or thermally [9, 11]. Although more difficult to design and build than hybrid devices, on-chip frames offer unparalleled frame/sample alignment, which is critical for a number of small-scale tests. The only drawbacks are lack of versatility (the size and shape of the sample cannot be readily changed) and limited displacement range (often $<$100 μm) [2, 11].

Versatile micro-test frames with large displacement capabilities inevitably require a hybrid design, consisting of an off-chip displacement actuator and an on-chip micro-fabricated load sensor. Both the force sensor and the displacement actuator are mounted on multi-DOF micro-stages, which enable alignment with the sample (figure 1). Off-chip displacement actuators are commercially available and cover a wide spectrum of resolution and range[3]. Conversely, the selection, design and manufacturing of the optimal force sensor are still active areas of research. MEMS load sensors capable of both steady-state and dynamic measurements are generally designed as compliant structures. They operate by measuring the deflection induced by the applied force in a structure of known stiffness. The structure deflection is measured visually (with an optical microscope, a SEM or a laser) [12], with piezoresistive elements [13] or capacitively [9]. The third option offers by far the best resolution (~1–10 nN). The major limiting factors of all compliant sensors are the low force range (~200 μN) and the need to tune the stiffness of the device to that of the sample, with resulting lack in versatility [9] (although interesting strategies for range tuning have been recently proposed [14]).

Sensors based on double-ended tuning forks (DETF) have the potential to increase both range and versatility, while retaining exceptional resolution. The working principle of DETF force sensors is the change in the natural frequency of vibration in a pair of parallel and connected beams upon application of an external axial force. DETF sensors deflect axially rather than laterally, hence exhibiting essentially infinite stiffness relative to the sample being tested and exceptional force range. From an operational perspective, the only quantity that needs to be measured is the resonance frequency of the out-of-phase vibration mode, which can be determined with great precision. DETF force sensors have been successfully demonstrated at the macro-scale [15]. MEMS DETF sensors have also been studied but their implementation was limited to on-chip accelerometers and gyroscopes [16, 17] and, recently, electrometers [18]. Designing a MEMS DETF force sensor capable of off-chip interfacing with the sample for a displacement-controlled mechanical experiment remains a challenge (particularly regarding elastic stability, misalignment compensation, fast and low-noise electronics and packaging). Figure 2(*a*) illustrates the potential benefits of the hybrid micro-test frame envisioned here, compared to existing concepts. The

[3] For example, the Newport VP-25XL single axis linear stage with controller (XPS-C2) and drive card (XPS-DRZ02) guarantees 25 mm displacement range and 5 nm resolution (www.newport.com).

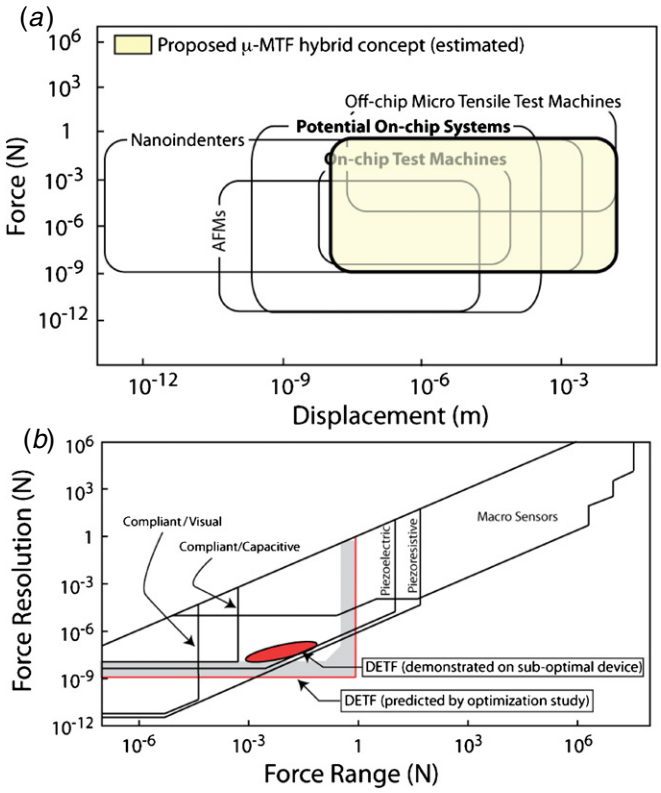


Figure 2. Comparison of commercially available sensors and actuators (modified from [2]). (*a*) Combinations of force and displacement ranges in micro-mechanical test frames. (*b*) Combinations of force range and resolution attainable by force sensors. The optimal design study presented in this paper suggests that previously unattainable combinations of force ranges (mN → N) and resolutions (nN → μN) are achievable with the proposed concept.

performance advantages of the DETF force sensor (in terms of resolution VS range) are depicted in figure 2(*b*).

The scope of this paper is fourfold: (i) to perform a comprehensive optimal design study for DETF force sensors and investigate the best attainable (non-trivial) combinations of resolution and range, (ii) to assess the dynamic range, which directly relates to the sensor versatility, (iii) to investigate the effect of air pressure on the performance of the sensor, thus assessing under which conditions vacuum operation is necessary and (iv) to demonstrate the concept (and the analytical approach) with one prototype.

The integration of the MEMS sensor and all the electronics within a compact PCB and the development of the entire micro-mechanical test frame (figure 1) will be presented in a separate work. The sensor described in this paper only detects axial forces (and eliminates transverse force components, as described in section 2). Conceptually, multi-axis sensing can be implemented, by using concepts similar to those presented in [14], but this extension is not presented here.

Although developed primarily as a load sensor within a micro-mechanical test frame, the sensor developed herein can be applicable to any situation where extreme combinations of force range, resolution and robustness are desirable: ranging from microgrippers [11] to force probes for endoscopic surgery [19, 20] and accelerometers.

The structure of the paper is as follows. Section 2 will present the proposed micro-mechanical test frame, describe the operational concept of the load cell and discuss its analytical model. In section 3, the geometric and electrical parameters of the load cell are optimized for resolution and range. The concepts developed in the paper are verified experimentally in section 4. Conclusions follow.

2. Modeling of an axially loaded resonant force sensor for micro-mechanical test frames

2.1. Schematic of the proposed design and operating principle

A schematic of the hybrid micro-mechanical test frame (μ-MTF) envisioned in this paper is depicted in figure 1. The proposed system comprises a DETF micro-load cell (inset in figure 1), an off-the-shelf displacement actuator capable of ∼10 nm resolution and ∼1 cm range[4], a 5 degree-of-freedom micro-positioning sample stage (Newport DS40-XYZ, GON40-U, GON40-L), a support/alignment rail and a camera with a long working distance lens (Infinity K2). A vacuum chamber complements the system to achieve maximum resolution.

With the exception of the force sensor, all the components in this system are available off-the-shelf; consequently, their performance and characterization are not discussed here. Figure 10 depicts the main components of the MEMS DETF sensor. In simplest terms, the tuning fork is driven to resonance with a sinusoidal voltage signal applied to a pair of electrodes (the drive electrodes). Care must be exerted so that the fork is modulated at the desired vibration mode. A separate pair of electrodes (the sense electrodes) senses a periodic change in the capacitor gap and responds with an ac current at the vibration frequency of the fork. Upon external axial force application, the natural frequency of the beam changes (figure 3), and this change is detected at the sensing electrodes (either by means of a feedback loop that adjusts the frequency to maintain the system at resonance or by tracking the amplitude change that corresponds to a deviation from resonance). The external force to be measured is applied axially to the DETF via a roller suspended on flexural springs (not shown in figure 10; see the inset in figure 1); the role of the roller is to eliminate the transmission of any transverse force component to the DETF, which would damage the tines and/or pollute the signal, while transferring the near totality of the axial component. The effectiveness of the roller is demonstrated with a finite elements sensitivity study (figure 4); for axial forces as large as 10 mN, the vibrational frequency of the tines is only modestly affected by transverse force components, up to very large misalignment angles (figure 4(*a*)). For applied axial forces in the range

[4] A vacuum compatible piezo-driven nano stage (Newport AG-LS25V6) is currently used, allowing 12 mm range and 50 nm step size (albeit with no feedback). For more accurate positioning, a better option is a stage with a feedback loop (e.g., Newport VP-25XL), guaranteeing 25 mm range and 5 nm resolution.

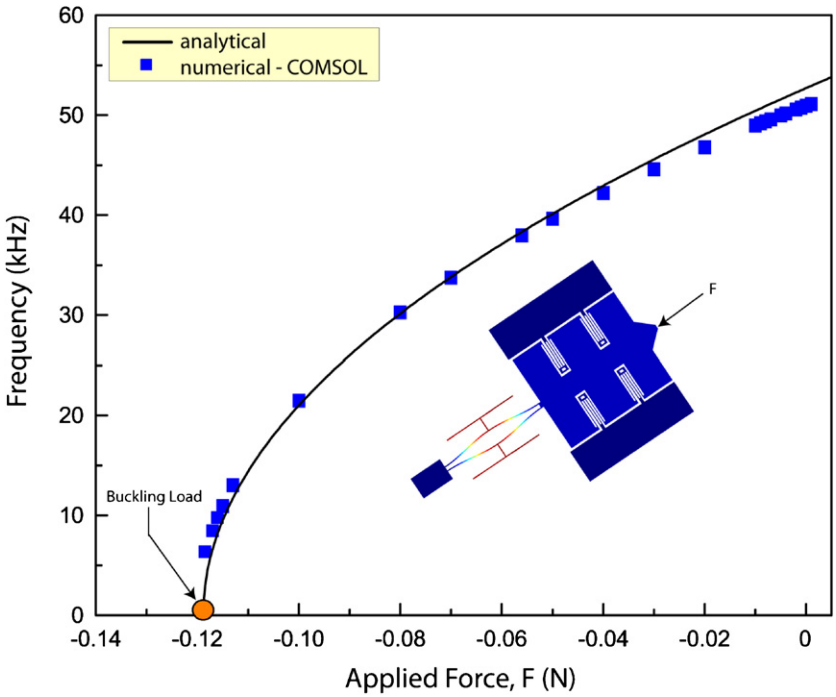


Figure 3. Change in natural frequency as a function of the applied axial load. The following dimensions were used (see figure 5 for nomenclature): $L_f = 964$ μm, $w_f = 10$ μm, $L_p = 680$ μm, $w_p = 10$ μm, $L_c = 120$ μm, $w_c = 10$ μm, device thickness, $h = 100$ μm, and gap, $g = 5$ μm. The analytical prediction agrees well with the finite elements results (obtained with COMSOL Multiphysics). Minor discrepancies are attributed to the presence of the roller.

10 μN $\rightarrow$10 mN, the device analyzed in figure 4 has a measured scale factor of $\sim$240.8 kHz N^{-1} (see section 4). The DETF interprets the frequency changes depicted in figure 4(*a*) as fictitious axial forces, which constitute an error on the axial force reading. Figure 4(*b*) shows the error amount as a function of the magnitude of the applied axial force and the degree of force misalignment. Note that the roller ensures that even at enormous force misalignments (over 20°) and large applied axial forces (10 mN), the error on the sensor reading is less than 1% (figure 4(*b*)). The implication is that the proposed device is extremely robust with respect to sample/sensor misalignment.

The resolution of the load cell depends primarily on three factors: the geometric dimensions of the device, the noise level of the electronic equipment and the amount of electrical and mechanical losses (expressed by the Q factor). Section 2.2 presents the mathematical derivations leading to force resolution and range. Finally, although the device represented in figure 2 is designed for compression (or bending) tests, simple modifications would allow it to operate in tension.

2.2. Electro-mechanical response of the MEMS stiff resonant load cell

The electro-mechanical behavior of DETF is well documented [16, 17]. Here we recall the main results. All the details are contained in appendix A.

The natural frequency of the tines for the first out-of-phase in-plane mode (figure 3) is given by $\omega_n = \sqrt{K_{\text{eff}}/M_{\text{eff}}}$, where the effective stiffness, K_{eff}, and the effective mass, M_{eff}, can be expressed as

$$K_{\text{eff}} = 192\frac{\text{EI}}{L_f^3} + 2.4\frac{F_{\text{appl}}}{L_f} - \frac{\varepsilon_0 h L_p}{g^3}\left(V_{\text{dc}}^2 + \frac{V_{\text{ac}}^2}{2}\right)$$
$$M_{\text{eff}} = \frac{13}{35}\rho\, h\, w_f L_f + \rho\, h(w_p L_p + w_c L_c). \quad (1)$$

Here, EI is the flexural stiffness of the tine for bending in the (x,y) plane, F_{appl} is the external axial force on the load cell (equal to twice the force applied on each tine), ρ is the materials mass density, A is the cross-sectional area of the tine, ε_0 is the dielectric constant of vacuum ($\varepsilon_{\text{air}} \sim \varepsilon_0$) and g is the actuation plate capacitor gap. All the other geometric parameters are defined in figure 5. Note that the applied axial force has a linear effect on the effective stiffness. The sensitivity of the device (defined as the frequency change corresponding to a unit change in applied force) is simply $\partial\omega_n/\partial F_{\text{appl}} = 1.2/(\omega_n M_{\text{eff}} L)$.

If the fork is driven at resonance electrostatically, with a signal $V(t) = V_{\text{dc}} + V_{\text{ac}}\cos(\omega_n t)$ (see the test schematic in figure 10), the output voltage is

$$P_e(t) = \frac{1}{2}\frac{\varepsilon_0 h L_p}{(g-y)^2}V^2(t) = \frac{1}{2}\frac{\varepsilon_0 h L_p}{(g-y)^2} \times \left[V_{\text{dc}}^2 + \frac{V_{\text{ac}}^2}{2} + 2V_{\text{dc}}V_{\text{ac}}\cos(\omega t) + \frac{V_{\text{ac}}^2}{2}\cos(2\omega t)\right], \quad (2)$$

where R_{amp} is the resistance of the trans-impedance amplifier, C is the capacitance of the condensers and Q is the quality factor of the signal. Any form of damping in the system

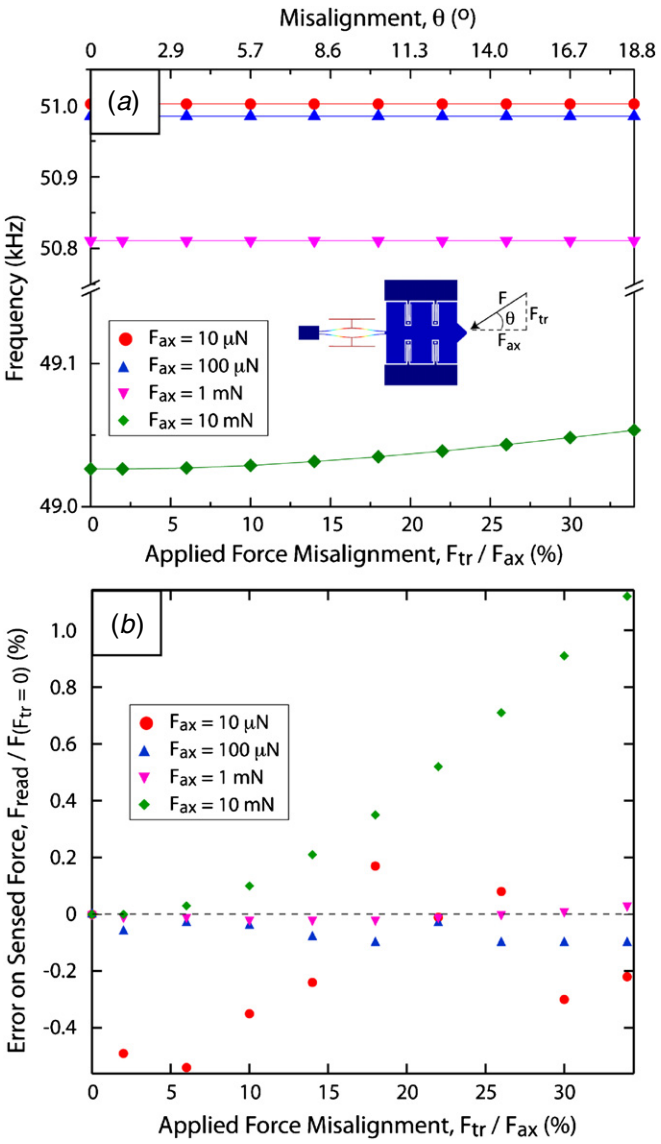


Figure 4. Finite elements analysis (COMSOL Multiphysics) showing the sensitivity of the DETF sensor to misalignment in the applied force. The sensor dimensions are the same as for figure 3. (*a*) Natural frequency change induced in the sensor as a function of the applied force misalignment. The axial force is kept constant, while a transverse force component is progressively increased. Results are provided for four different values of the axial force. (*b*) Error on the axial force sensed by the DETF as a function of the applied force misalignment. The data are obtained by (*a*) using the experimentally measured scale factor of 240.8 kHz N^{-1}. Note that even substantial misalignments (∼30%) and a large applied axial force (10 mN) induce less than a 1% error in the sensor reading.

will lower the natural frequency [21], but this effect is only significant for $Q < 2$. As estimated Q factors for optimized devices are at least of the order of $Q \sim 10$ (even at atmospheric pressure), undamped frequencies will be used throughout this work.

2.3. Noise estimation and minimum detectable force

We assume that the output voltage (obtained by grounding the output current through the trans-impedance amplifier resistance—figure 10) be subjected to a white noise, V_{noise}, given by the Johnston–Nyquist thermal noise [22] and the trans-impedance amplifier noise:

$$V_{\text{noise}} = \sqrt{4k_B T\, R_{\text{amp}} + e_n^2 + R_{\text{amp}}^2 i_n^2}\sqrt{\Delta f}, \tag{3}$$

where Δf is the bandwidth over which the noise is measured (for the optimization work in section 3, $\Delta f = 100$ Hz[5]), R_{amp} is the resistance of the trans-impedance amplifier, e_n and i_n are the input voltage and current noise of the amplifier, respectively, k_B is the Boltzmann constant and T is the absolute temperature. For a commercially available low-noise operational amplifier (e.g., AD549), the intrinsic noise figures can be as low as $e_n = 35\ nV/\sqrt{\text{Hz}}$, $i_n = 0.016\,fA/\sqrt{\text{Hz}}$. This voltage noise results in a phase noise for the system, $\Delta\omega_{\text{noise}}$. With conservative estimates (appendix B), the minimum resolvable force in the presence of this noise (i.e. the force resolution) can be expressed as

$$F_{\text{min}} = F_{\text{noise}} = \frac{\Delta\omega_{\text{noise}}}{\partial\omega_n/\partial F_{\text{appl}}} = \frac{1}{\partial\omega_n/\partial F_{\text{appl}}}\frac{\omega_n}{2Q}\arctan\left(\frac{V_{\text{noise}}}{V_{\text{out}}}\right). \tag{4}$$

2.4. Q factor estimation

The Q factor in equation (4) is a strong function of the ambient pressure and packaging quality. At atmospheric pressure, viscous damping from the air in small gaps is a dominant source of loss for resonators. As the air pressure is reduced, this damping effect rapidly drops and mechanical losses through the substrate become the limiting factor [23]. Cognizant of this difference, we adopt two different approaches for Q estimation: one representative of operation at atmospheric pressure and one for vacuum operation ($p <$ 100 mTorr).

Operation in air ($p = 760$ Torr (1 atm)). Under atmospheric pressures, the air in the gap acts both as a damper and as a spring. The relative amounts depend on the compressibility of the fluid, expressed by the squeeze number [24, 25]:

$$\sigma = \frac{12\,\mu h^2\omega_n}{Pg^2}, \tag{5}$$

where $\mu = 17.9 \times 10^{-6}$ Pa s and $P = 1.01 \times 10^5$ Pa are the viscosity and pressure of air, respectively, and h and g are the device thickness and the gap width, as defined before. The larger the squeeze number, the more pronounced the compressibility effects. The damping coefficient can be expressed as [24, 25]:

$$c \sim 2\frac{64\,\sigma P L_p h}{\pi^6\omega_n g}\frac{1+(h/L_p)^2}{[1+(h/L_p)^2]^2+\sigma^2/\pi^4}, \tag{6}$$

where the factor 2 accounts for damping on both the driving and sensing side.

[5] Large bandwidths allow for dynamic measurements at high strain rates and are obviously desirable. At the same time, increasing the bandwidth also increases the noise (figure 13(*b*)). A value of 100 Hz was chosen as a reasonable compromise.

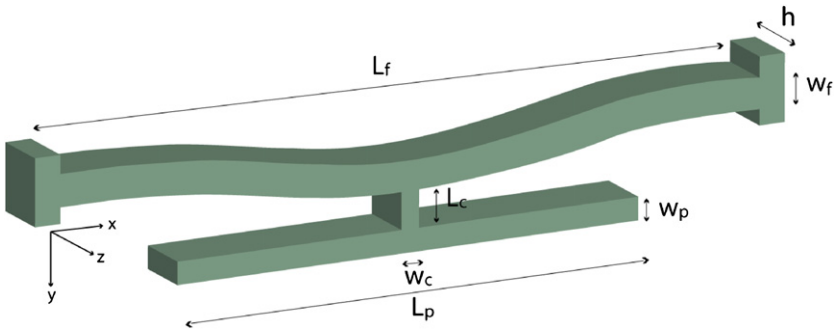


Figure 5. Geometry and variables definition for a simple tine with an actuation plate at the center. The dynamics of the tine is analyzed with a lumped mass–spring-damper model.

Similarly, the spring constant of the air is given by [24, 25]

$$K_{\text{air}} \sim 2\frac{64\,\sigma^2 P L_p h}{\pi^8 g}\frac{1}{[1+(h/L_p)^2]^2+\sigma^2/\pi^4}. \qquad (7)$$

Note that the air spring constant is a strong function of the operational frequency. This term must be added to the electromechanical spring stiffness for a correct estimation of the frequency of the out-of-plane mode. Once the frequency is found, the Q factor is immediately derived as $Q = M_{\text{eff}}\omega_n/c$. The accuracy of this model was verified against experimental results, which are presented in section 4.

Operation in vacuum ($p < 100$ mTorr). As the air pressure is decreased, viscous damping in the gap becomes less and less significant and the energy loss is ultimately governed by packaging-level factors (compliance of the chip/package adhesive, vibration of the package, vibration of the surrounding frame, etc). As these factors are extremely difficult to predict analytically, we choose to measure the damping coefficient experimentally. For the device described in section 4, we obtained: $c_{\text{vac}} = 3.95 \times 10^{-7}$ Nsm^{-1} at a vacuum level of 50 mTorr (corresponding to $Q \sim 1800$). Further decreasing the pressure by a factor 10 only marginally affected c (a 50-fold reduction only yielded $Q \sim 3000$). Hence this value is taken as a measure of the system (non-viscous) loss coefficient. It should be emphasized that much larger Q values can be achieved with more careful packaging, but in the present feasibility study, $c_{\text{vac}} = 3.95 \times 10^{-7}$ Nsm^{-1} will be adopted throughout for conservativeness. Assuming that c is not affected by the device geometry (a reasonable assumption for device masses much smaller than the package mass), a quality factor Q for vacuum operation is obtained as $Q = M_{\text{eff}}\omega_n/c_{\text{vac}}$.

3. Optimal design

3.1. Free variables, objective functions and constraints

3.1.1. Variables. The geometry of the load cell is entirely defined by the device thickness, h, the capacitors' gap, g (assumed the same for all capacitors), the tines' width, w_f, and length, L_f, and the driving plates' length, L_p (figure 5). Three additional geometric variables exist (driving plate width, w_p, connector width, w_c, and connector length, L_c); as they only affect the mass of the structure and not its stiffness (and in turn reduce the sensitivity), they should be as small as possible without decreasing the stiffness of the driving plates excessively (which would result in nonlinearities in the voltage–force relationship). We choose $w_p = w_c = 10$ μm (this value is inferred from finite elements simulations to ensure rigidity of the actuation plates during operation) and $L_c = 4g + 2w_p$ (to allow for positioning of the driving and sensing electrodes). The free geometric variables summarized above are bound by realistic manufacturing constraints. Additionally, the driving voltages (V_{dc} and V_{ac}) can also vary within reasonable bounds. The total list of free variables and their allowed ranges are reported in table 1.

Table 1. List of variables with relative bounds in the optimization problem.

Free variable (unit)	Symbol	Lower Bound	Upper Bound
Tine length (μm)	L_f	50	1000
Tine width (μm)	w_f	5	15
Driving plate length (μm)	L_p	40	800
Capacitors gap (μm)	g	2	20
Driving dc voltage (V)	V_{dc}	1	40
Driving ac voltage (V)	V_{ac}	0.01	10
Fixed variable (unit)	**Symbol**	**Value**	
Driving plate width (μm)	w_p	10	
Connector width (μm)	w_c	10	
Connector length (μm)	L_c	$4g + 2w_p$	
Device thickness (μm)	h	25, 50, 75, 100	

3.1.2. Objective function. The objective of this analysis is the design of a micro-load cell with maximum values of force resolution (equation (4)) and range (defined as the maximum tensile or compressive force that can be safely applied without permanently damaging the structure). The two objectives are obviously competitive (e.g., the thinner the tine, the higher the resolution and the lower the limit load). The solution to this multi-objective optimization problem can be conveniently expressed in terms of a *Pareto frontier* [26], defined as the set of solutions where the value of one objective cannot be improved without a detrimental effect on the other objective.

Table 2. List of constraints for the optimization problem.

Constraint	Equation	Index
Geometric/manufacturing constraints		
Limit on actuation plate length	$L_p \leqslant 3L_f/4$	(a)
DRIE limit on a vertical aspect ratio	$h \leqslant 15 \cdot g$	(b)
SOIMUMPS limit on a in-plane aspect ratio	$L_f \leqslant 100 \cdot w_f$	(c)
	$L_p \leqslant 100 \cdot w_p$	(d)
Electro-mechanical constraints		
No static pull-in	$V_{\mathrm{dc}} \leqslant \sqrt{K_{\mathrm{eff}} g^3/2\varepsilon_0 h L_p}$	(e)
No resonant pull-in	$V_{\mathrm{dc}} V_{\mathrm{ac}} \leqslant (\pi K_{\mathrm{eff}} g^3) \cdot (6\sqrt{3} Q \varepsilon_0 h L_p)^{-1}$	(f)
Structural robustness constraints		
No yielding	$F_{\max} \leqslant 2\sigma_Y h w_f$, with $\sigma_Y = 5$GPa	(g)
No in-plane buckling (compression only)	$F_{\max} \leqslant 2\pi^2 E\ h\ w_f^3/3L_f^2$	(h)
No out-of-plane buckling	$h > 2w_f$	(i)
No fracture (tension only)	$F_{\max} \leqslant 2\sigma_f h w_f$, with $\sigma_f = 3$GPa	
Linearity constraints		
Upper bound on vibration amplitude	$y(t) \leqslant \min\{g/10, w_f/25\}$	(j)
Noise constraints		
Lower bound on natural frequency	$\omega_n/2\pi > 10$kHz	(k)
Upper bound on natural frequency	$\omega_n/2\pi \leqslant 300$kHz	(l)
Lower bound on output signal voltage	$V_{\mathrm{out}} \geqslant 1$ mV	(m)

The implementation with two objectives is straightforward: feasible values of the force range are discretized in the interval $-1 \rightarrow 0N$ (future assessment will present results for tensile loads), and for every feasible value in the domain the force resolution is optimized. With this approach, the mechanical resistance of the tines to buckling, yielding and fracture becomes a constraint, thus reducing a two-objective problem to a single-objective problem. The objective function is then simply equation (4).

Note that the resolution is affected by the applied force. As the buckling limit of the device is approached, the resolution increases, while it decreases for tensile forces. As we are interested in a conservative estimate of the resolution valid over the entire range of applied (typically compressive) forces, in the optimization routine we will evaluate the resolution at $F_{\mathrm{appl}} = 0$.

3.1.3. Constraints. The various constraints affecting the optimal design are briefly discussed below. All the formal expressions are reported in table 2.

Geometric or Manufacturing requirements. To ensure compatibility with the standard SOIMUMPS process for MEMS fabrication [27], all dimensions (including gaps) are constrained to be larger than 2μm. To allow insertion of the roller depicted in the inset of figure 1, the length of the actuation plates is constrained to be smaller than 75% of the length of the tines. Limitation on microfabrication equipment imposes additional constraints: (i) conventional deep reactive ion etching (DRIE) systems achieve their best profiles with aspect ratios lower than 15:1. (ii) Based on the SOIMUMPS design rules [27], the length of the fork is related to its width to avoid possible fracture upon release of the structure: it is recommended that cantilever beams have a maximum in-plane aspect ratio 100:1.

Electrostatic/electrodynamic requirements. The dc and ac voltages required to drive the device are constrained by the pull-in condition (i.e. the condition at which the attractive electrostatic force between two charged plates overcomes the repulsive elastic force exerted by the springs) [23, 28].

Structural integrity requirements. Assuming sufficient ductility, for applied tensile forces the tuning fork can only fail by yielding ($\sigma_Y = 5$ GPa is the yield strength of silicon in the (1 1 1) plane [29, 30]). Even for the small tine cross-section, this constraint would only become active at extremely large forces (for $h = 10\ \mu$m, $w_f = 5\ \mu$m, the maximum force per tine would be 0.25 N). The choice of [1 1 1] silicon wafers simplifies the mechanical analysis considerably, as the (1 1 1) plane is a plane of isotropy (i.e. properties are the same along any direction normal to [1 1 1]) [29, 30]. Under tensile forces, failure may occur by fracture rather than yielding. The fracture strength of single-crystal silicon is strongly affected by specimen size, processing condition and coatings. Fracture strengths larger than $\sigma_f = 3$ GPa have been consistently measured experimentally [31, 32], although lower values are possible in the presence of sharp corners (typically induced by anisotropic etching), which can introduce considerable stress concentration factors. In the present work, it is assumed that sharp corners can be avoided, and we use $\sigma_f = 3$ GPa as the maximum allowable stress in tension. Under applied compressive forces, the tuning fork may fail by buckling. The roller connected to the tip of the DETF (inset in figure 1) ensures that the tines buckle as clamped-clamped beams. To ensure that out-of-plane buckling modes have higher critical loads (and hence can be safely ignored), we additionally impose the constraint: $h > 2w_f$.

Linearity requirements. The actuation force at the capacitor plates is dependent on the plate displacement (see appendix A). In order to avoid nonlinearity at the sense

electrode, the maximum lateral displacement of the beam during actuation is prescribed to stay below 10% of the capacitor gap. Similarly, to ensure applicability of linear beam theory, the maximum lateral displacement is prescribed not to exceed 4% of the tine width.

Constraints on noise level. The oscillation frequency of the fork is prescribed not to exceed 300 kHz (to avoid excessive gain loss at the trans-impedance amplifier) and the output signal, V_{out} is required to be larger than 1 mV to ensure effective signal processing.

3.2. Optimal design procedure

The objective of the optimization process is to maximize the resolution of the device (i.e. minimize the minimum detectable force) as a function of the desired force range, F_{appl}. As the device thickness is often dictated by the available SOI/SOG technologies and the manufacturing process (e.g., SOIMUMPS), here it is taken as a discrete parameter as opposed to as a variable; optimal designs are extracted for four common values of the device thickness: 25, 50, 75 and 100 μm. The large number of variables and constraints and the nonlinear nature of objective function and constraints require the use of efficient numerical optimizers. The problem stated above is solved using a particle swarm optimization (PSO) scheme. This technique is discrete and does not require the calculation of gradients. It has been proven to work well in problems defined by a large occurrence of local optima. Details of the algorithm are presented in appendix C and [33].

3.3. Results

The maximum resolution of the device (i.e. the minimum applied force that can be discerned from the noise) is plotted in figure 6 for air and vacuum operation, as a function of the desired force range. Results are presented for four different levels of the device thickness. Every point on each curve represents a *specific design*, expressed by a set of geometric parameters (elaborated below). Note that increasing the device thickness always (not surprisingly) extends the range (by retarding the onset of the buckling constraint). For operation in air, this is accompanied by a decrease of the device resolution, but the converse is true in vacuum. The interesting implication is that in vacuum thicker devices are preferable in terms of both resolution and range.

The values of each geometric parameter that fully defines the optimal designs depicted in figure 6 are presented in figure 7 (for device thicknesses of 25, 50 and 100 μm; note that the scale on the x-axis is different for each thickness). Note that for vacuum operation the optimal device dimensions are nearly constant across the entire spectrum of allowable force ranges. This finding has significant implication for the resonant load cell designer, as most particular designs are optimal for *any* desired force range.

While several variables choose to attain upper or lower bounds for the entire spectrum of force ranges, others (most typically the tine and sensing/detection plate length, the tine

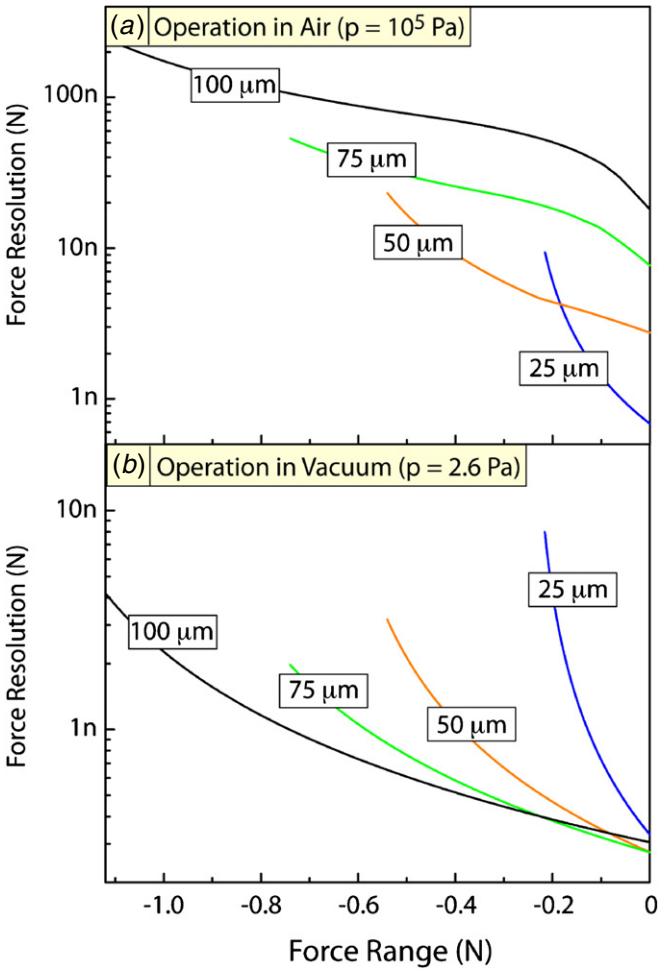


Figure 6. Force resolution VS force range for optimized resonant micro-load cells: (*a*) operation in air and (*b*) vacuum. Four different device thicknesses are depicted. Increasing the device thickness increases the force range, but in air this is accompanied by a substantial decrease in resolution. Interestingly, for vacuum operation, thicker devices are generally more sensitive.

width, the gap size and the imposed ac voltage) often take non-trivial optimal values. To elucidate the physics behind these optimal dimensions, the 'activity' of each constraint is plotted in figure 8. A constraint activity parameter of 0 signifies an active constraint; any value lower than 0 means that the constraint has no effect on the optimal geometry. As an example, the constraint activity parameter for buckling is defined as $\Pi_{buckling} = P_{appl}/P_{buckl} - 1$. Inspection of figures 7 and 8 immediately illustrates the constraints that influence the optimal geometry and the individual variables that are affected by them. The results are reported in table 3 and can be summarized as follows.

(i) For thin devices ($h = 25$ μm), four variables attain non-extremal values, governed by four active constraints. In this case, the variables/constraints relationship is clear: the tine thickness, w_f, is dictated by the condition $h > 2\,w_f$; the tine length, L_f, is chosen not to violate the upper bound on resonant frequency ($\omega_{n,max}/2\pi < 300$kHz) and vibration amplitude ($y_{max} < \min\{g/10,\ w_f/25\}$);

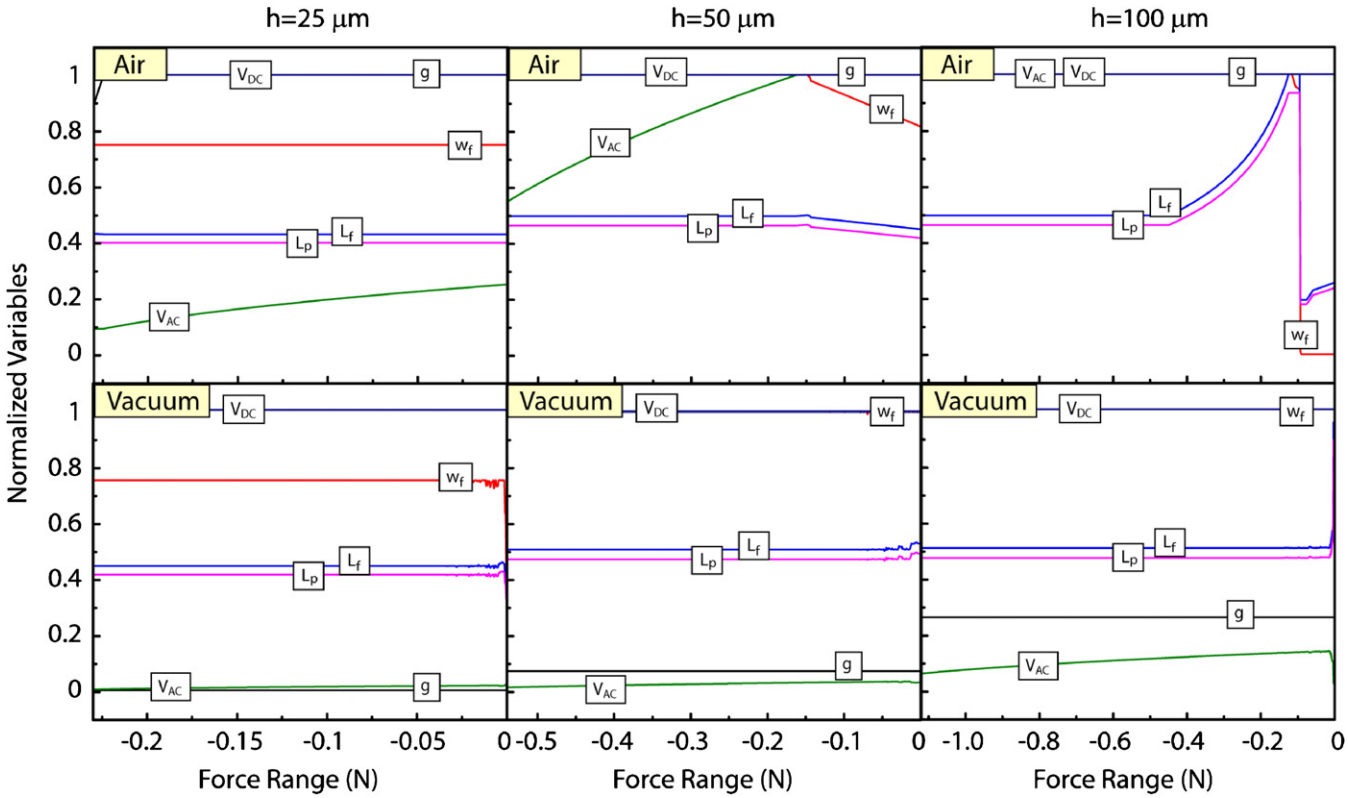


Figure 7. Optimal values of the geometric and electric parameters result in the performance depicted in figure 6. Results are presented for air and vacuum operation, for three values of the device thickness. All variables are normalized in a 0–1 range, with 0 indicating the lower bound and 1 the upper bound (see table 1).

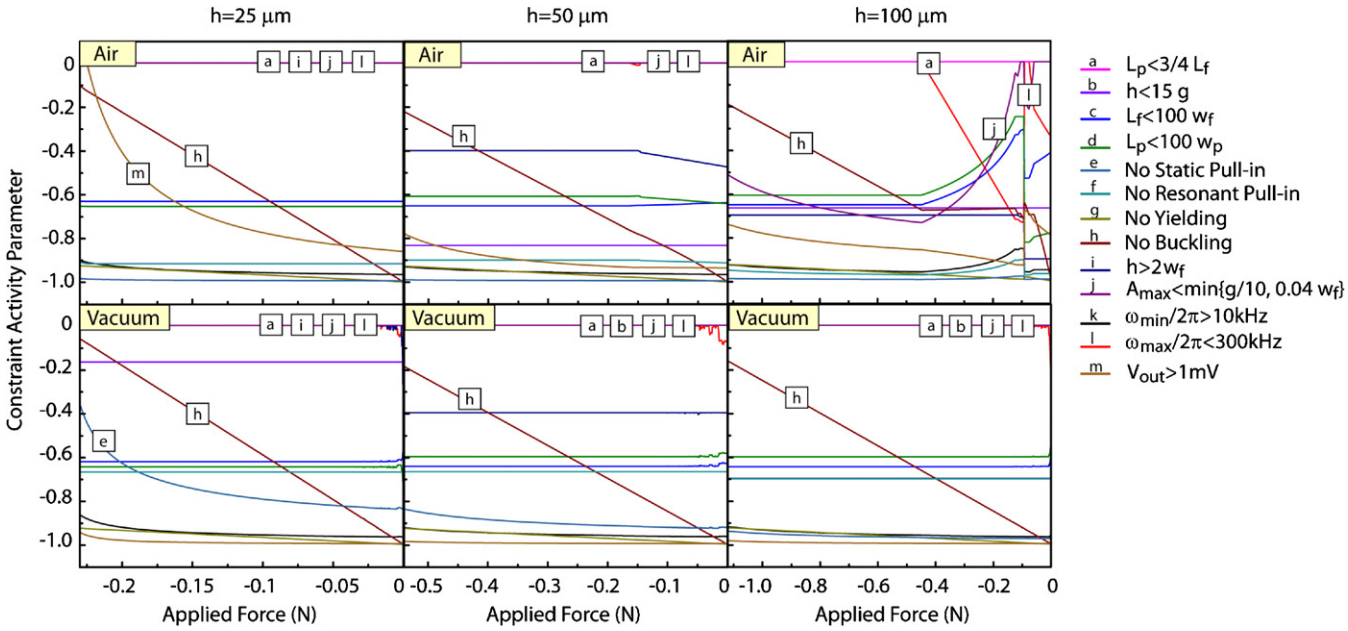


Figure 8. Relative contribution of all constraints to the optimal design depicted in figure 7. Positive values would indicate constraints violations and are thus ruled out by the optimizer. A constraint activity parameter of 0 indicates that the constraint is active, whereas all negative values designate inactive constraints.

Table 3. Summary of optimal variable values and limiting constraints.

		$h = 25\ \mu$m		$h = 50\ \mu$m		$h = 100\ \mu$m	
		Optimal value	Limiting constraint	Optimal value	Limiting constraint	Optimal value	Limiting constraint
				AIR			
Free variables	L_f	460 μm	(l); (j)	RD[a]	(l); (j)	RD[a]	(l); (j)
	w_f	12 μm	(i)	RD[a]	(l); (j); UB[a]	RD[a]	(l); (j); UB[a]
	L_p	345 μm	(a)	RD[a]	(a)	RD[a]	(a)
	g	20 μm	UB[a]	20 μm	UB[a]	20 μm	UB[a]
	V_{dc}	40 V	UB[a]	40V	UB[a]	40V	UB[a]
	V_{ac}	RD[a]	(j)	RD[a]	(j)	10V	UB[a]
				VACUUM			
Free variables	L_f	472 μm	(l); (j)	533 μm	(l); (j)	531 μm	(l); (j)
	w_f	12 μm	(i)	15 μm	UB[a]	15 μm	UB[a]
	L_p	354 μm	(a)	399 μm	(a)	398 μm	(a)
	g	2 μm	LB [a]	3.33 μm	(b)	6.67 μm	(b)
	V_{dc}	40 V	UB[a]	40V	UB[a]	40 V	UB[a]
	V_{ac}	RD[a]	(j)	RD[a]	(j)	RD[a]	(j)

[a]RD = range dependent; UB = upper bound; LB = lower bound. Constraint index defined in table 2.

the length of the capacitor plate is related to the tine length by $L_p < (3/4)L_f$; and the applied ac voltage, V_{ac}, is limited to ensure small vibration amplitudes (i.e. $y_{max} < \min\{g/10,\ w_f/25\}$).

(ii) For thicker devices in vacuum ($h = 50\ \mu$m, $h = 100\ \mu$m), the situation is identical to case (i) for L_f, L_p and V_{ac}. The constraint $h > 2\ w_f$ is no longer active, and consequently the tine width, w_f, attains its upper bound; in this case, though, the capacitor gap, g, takes non-extremal values and is controlled by the active constraint: $h < 15g$.

(iii) For intermediate thickness devices in air ($h = 50\ \mu$m), the non-extremal variables are the same as for case (i), but no aspect ratio constraint is active. Consequently, L_p is governed by the condition $L_p < (3/4)L_f$, L_f and w_f are determined by the upper bound on the resonant frequency, $\omega_{n,max}/2\pi < 300$ kHz and vibration amplitude, $y_{max} < \min\{g/10,\ w_f/25\}$ and V_{ac} is solely determined by the upper bound on the vibration amplitude.

(iv) For thick devices in air ($h = 100\ \mu$m), only two variables attain non-extremal values: the tine and capacitor lengths, L_f and L_p. The former is determined by the upper bound on the resonant frequency ($\omega_{n,max}/2\pi < 300$ kHz), whereas the latter is once again related to L_f by the condition $L_p < (3/4)L_f$. At small-medium force range, the upper bound on the resonant frequency is not active and consequently the lengths are free to vary as a function of the range to maximize the resolution. Finally, for very small force ranges, the constraint on vibration amplitudes is active: under these conditions, both the optimal fork length and width attain much lower values.

For all the conditions analyzed in this work, the applied dc voltage is always at the upper bound. The behavior of the capacitor gap is more interesting and at first counterintuitive. For vacuum operation, the gap tends to choose the lowest possible values, to maximize the resolution. Note, though, that the converse is true for air operation. The reason for this apparent contradiction lies in the different assumptions in the calculation of the Q factor. (a) In vacuum, the damping coefficient, c, is independent of the device geometry and the gap size. Consequently, the gap is minimized to

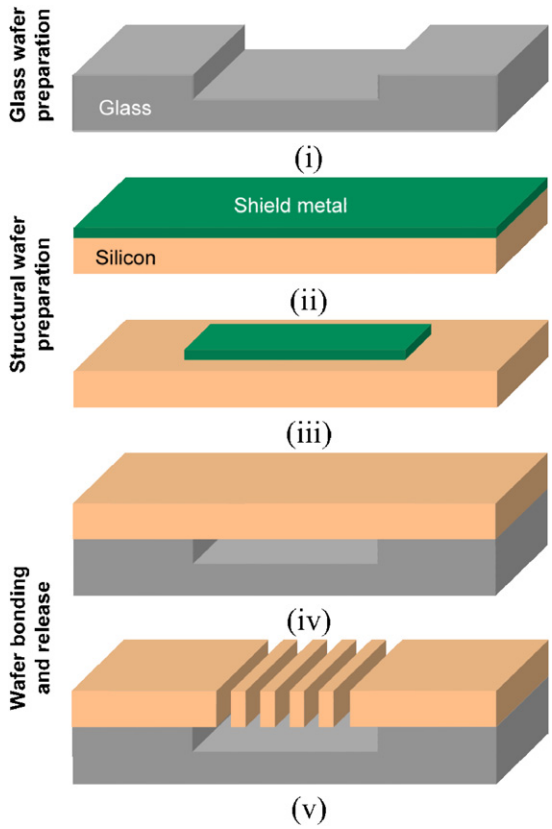


Figure 9. Schematic of the silicon-on-glass (SOG) manufacturing approach (modified from [34]).

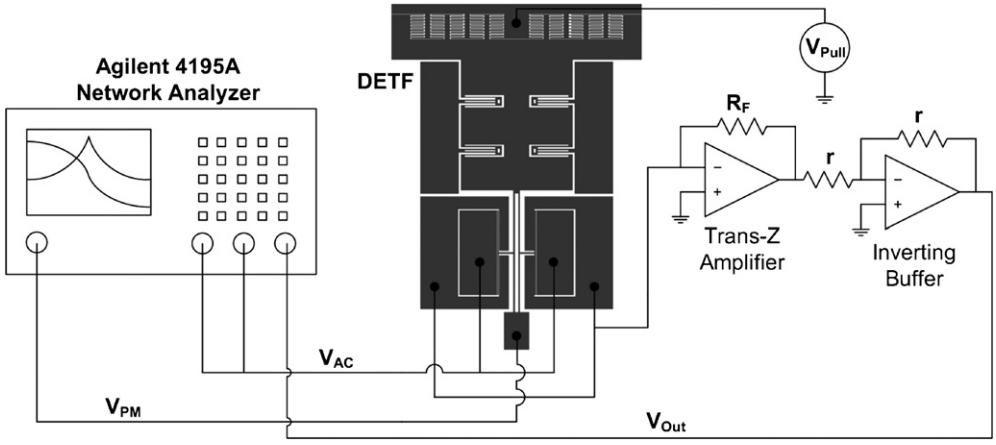


Figure 10. Experimental set-up for the characterization of the resonant load cell. The roller of the load cell is connected to a parallel-plate electrostatic actuator to facilitate calibration. In one characterization procedure, the actuator was used to apply a force to the load cell (in tension), whereas in another scheme the entire set-up was rotated to subject the load cell to a well-controlled variable g-force.

optimize the resolution, and Q is maximized by selecting dimensions yielding large natural frequency and mass. (b) In air, a large gap is preferred to reduce the viscous dissipation, which for small squeeze numbers scales as g^{-3} (equation (6)). The important implication is that large-gap designs can be chosen for air operation resulting in exceptional resolutions: significantly expanding the applicability of the proposed concept.

Finally, note that the buckling constraint is never active for any value of the force range. The activity parameter for the buckling constraint, though, steadily rises as the range in extended (figure 8). The activation of the buckling constraint indicates the end of the feasible load range, for all the optimization studies performed in this work.

4. Experimental verification

4.1. Microfabrication approach

The MEMS load cell depicted in the inset of figure 1 was microfabricated with a well-established silicon-on-glass (SOG) process (figure 9) developed at the MEMS Center, Middle East Technical University, as explained in [34][6]. In synthesis, device anchors are defined in the glass substrate by etching $\sim$10 μm deep recesses using pure hydrofluoric acid, with a 100 Å/2000 Å thick evaporated Cr/Au masking layer. The Cr/Au layer is stripped using commercial wet etchants. The structural wafer is a 100 μm thick silicon wafer. A 3700 Å thick Al layer is evaporated on the structural silicon wafer and patterned as the shield metallization layer in order to avoid ion damaging and overheating problems during DRIE of the silicon wafer. The surface of the structural wafer with shield metallization is anodically bonded to the glass substrate. Features in the Si wafer are defined by DRIE, followed by selective removal of the shield metallization, by means of a commercially available aluminum etchant.

[6] The process used here differs from [17] only in that it lacks the gold layer.

4.2. Experimental setup and results

The performance of MEMS resonant load cells described in section 2 was experimentally verified. A test load cell (figure 10) was manufactured as described in section 5.1, with the following dimensions (see figure 5): device thickness, $h = 100$ μm, tine length, $L_f = 964$ μm, tine width, $w_f = 10$ μm, gap, $g = 5$ μm, capacitor plate length, $L_p = 680$ μm, capacitor plate width, $w_p = 10$ μm, connector length, $L_c = 120$ μm, and connector width, $w_c = 10$ μm. Two quantities were carefully measured: the sensitivity of the device to an axially applied load (in terms of frequency change in the tines induced per unit force) and the minimum applied force that can be detected (i.e. the resolution of the device). Two complementary approaches were adopted for the application of a controlled axial load:

(i) A mass suspended by flexural springs was embedded in the chip and connected to the vibrating tines (figure 10). The whole chip was rotated by 360° along its out-of-plane axis, thus applying a variable force to the tines (equal to the weight of the suspended mass times the cosine of the angle between the tines and the vertical direction). Both tensile and compressive forces are possible, depending on the angle. The applied forces can be accurately controlled, but only small forces can be applied ($F_{\max} \sim 3$ μN).

(ii) An electrostatic force was applied by a bank of parallel plate actuators, embedded in the suspended mass (figure 10). With this approach, larger forces can be applied (although only in tension), but the control on the force was much less accurate than for approach (i), possibly due to dimensional imperfections in the gap size for the parallel plate actuator.

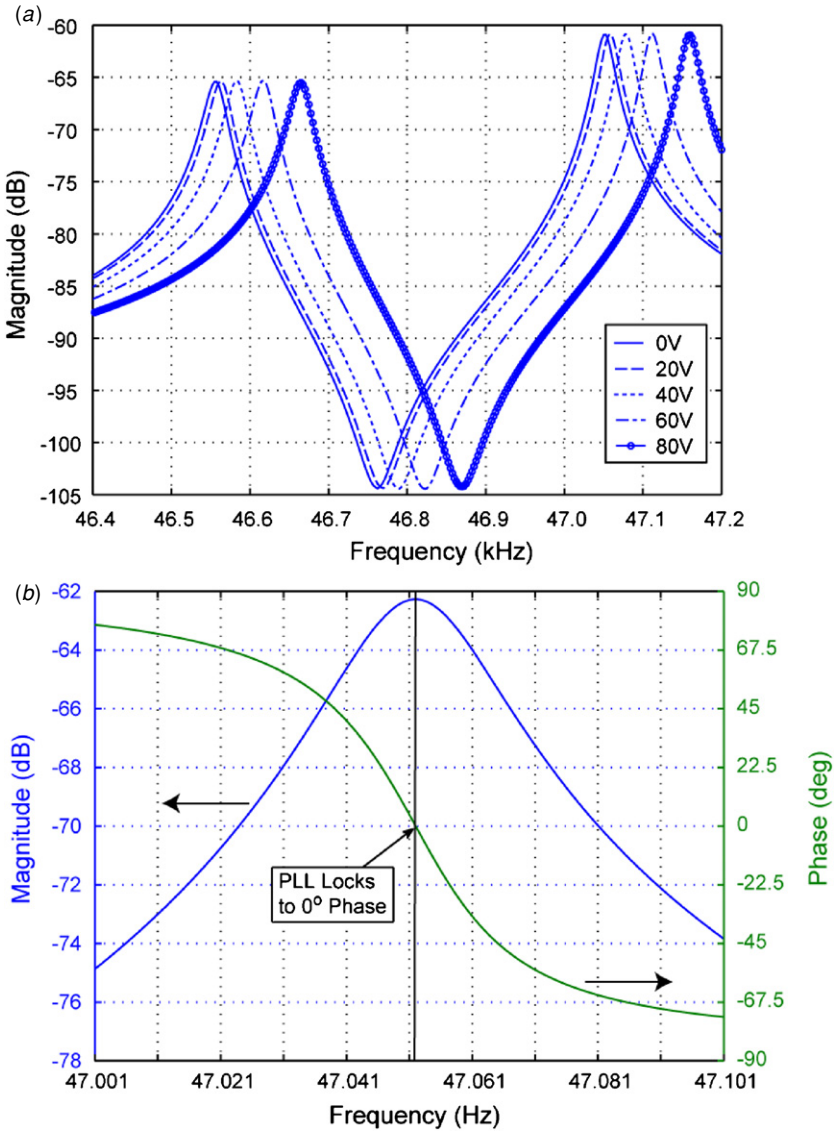


Figure 11. Experimental characterization of the resonant load cell. (*a*) Frequency sweeps (raw data) at different pulling voltages. (*b*) Operation point of the software-implemented PLL circuit.

The same experimental setup was used for both approaches (figure 10). All tests were run in a vacuum chamber, at p $\sim$ 50 mTorr. Excitation and detection were both controlled by a suitably programmed Network/Spectrum/Impedance Analyzer (Agilent 4195A).

The natural frequency in the absence of applied load was initially measured with a frequency sweep (figure 11(*a*)). The proof mass was biased to 40 V ($V_{\mathrm{PM}} = 40$ V) and an excitation signal of 10 mV ($V_{\mathrm{ac}} = 10$ mV) was adopted; the feedback resistance of the trans-impedance amplifier was 1 MΩ ($R =$ 1 MΩ). Note that the frequency response of the resonator exhibits two peaks, each corresponding to a distinct mode of vibration. The low-frequency peak corresponds to an in-phase motion of the tines (and is thus undesired), whereas the higher frequency peak corresponds to the predicted out-of-phase motion. Although every effort was made to suppress the in-phase mode (by shorting the capacitors on both tines), we were not able to eliminate it, possibly due to cross coupling between the plates and mismatched plate capacitances due to fabrication imperfections. However, both peaks exhibit nearly the same sensitivity to applied loads (represented by different values of the pulling voltage, see figure 11(*a*)), indicating proper operation of the resonator. Importantly, these peaks are not separable in low-Q conditions, indicating that air operation is only viable if the structure is perfectly balanced.

For a continuous tracking of the resonance frequency as a function of the applied load, a phase locked loop (PLL) was implemented within the analyzer. Figure 11(*b*) shows the operation point of the software implemented PLL. Knowing the phase between the driving and sensed signals (which is 0° for the given readout scheme), the analyzer performs single point frequency analysis and continuously shifts the excitation frequency to minimize the phase lag between input and output

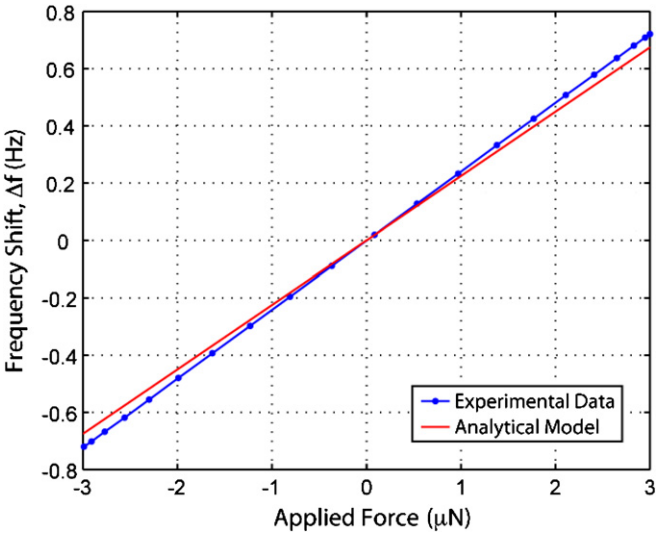


Figure 12. Natural frequency shift as a function of the applied force. Experimentally, the force is applied by gravity as the device depicted in figure 10 is rotated through a 2π angle. This technique allows very accurate measurements in both tension and compression, albeit at a very small range (the maximum applicable force is 2.99 μN, corresponding to 1 g). Note that the experimentally verified behavior is extremely linear, and agrees very well with the predictions from the analytical model. The measured scale factor of the resonator is 240.8 kHz N^{-1}, versus a predicted value of 224.8 Hz N^{-1}.

signals, thus keeping the system at resonance—see section 2.2 and appendix A).

The sensitivity of the device (in Hz N^{-1}) was measured using approach (i) above. The weight of the suspended mass was 2.99 μN. Data points were collected by rotating the sensor normal to the gravity field, with the analyzer locking the system to resonance. In this small force range, the response of the load cell is nearly linear, with a measured sensitivity of 240.8 kHz N^{-1}. The result agrees very well with an analytical value of 224.8 kHz (figure 12). The difference is likely attributable to some degree of undercut arising from the DRIE process, which alters both mass and stiffness (with a stronger effect on the latter).

To determine the resolveable tip loading (i.e. the resolution of the load cell), measurements were logged for 18 h with a sampling time of 1.3 s per data point, with the sensor stationary and unloaded. Figure 13(*a*) shows the output drift of the micro-load cell. The root Allan variance of the collected drift data [35, 36] is presented in figure 13(*b*). Because of logging and I/O delays inherent in the network analyzer, a programmed electronic bandwidth of 100 Hz resulted in a minimum processing time of ∼1.3 s. Under these conditions, we measure a resolution of 63 nN. For comparison, the analytical model presented in section 2.2 predicts a resolution of ∼4.5 nN for this specific sub-optimal device at a bandwidth of 100 Hz. This order of magnitude difference is not surprising and is consistent with the existence of noise sources not accountable for in the analytical model (and responsible for the rise of the Allan variance at large sampling times). Note that a slower sampling time would result in a measured resolution of ∼23 nN. Because of the substantial delay exhibited by the network analyzer, the time scale on the Allan variance plot (figure 13(*b*)) is not particularly meaningful. A purely analog readout circuit implemented entirely on a PCB that contains the package is currently being developed and will resolve this difficulty. The important conclusion emerging from this analysis is that the simplistic noise model at the basis of the optimization work presented in this paper is accurate within roughly an order of magnitude. Given the exceptional resolutions predicted analytically (figure 6), this confirms that resonant micro-load cells are exceptional candidates for ultra-sensitive and robust force sensors, even under significant loads.

5. Conclusions and future work

A novel hybrid micro-mechanical test frame based on a microfabricated resonant load cell and an external displacement actuator has been proposed for mechanical characterization of small-scale structures. The MEMS load cell has been designed, optimized for maximum force resolution and range, and experimentally demonstrated. The analytical/numerical models reveal that force resolutions on the order of a few nN are possible in vacuum, even for very large force ranges (∼0.1–1 N). Simple design improvements currently under considerations could result in sub-nN resolutions. A finite elements analysis confirms that the proposed sensor design is extremely robust with respect to sample/sensor misalignment, a necessary requirement for successful integration in an off-chip hybrid micro-load cell. Designs for vacuum operation are exceptionally versatile, as the same geometry is optimal for nearly any value of the desired force range. This allows one single device to be used for a variety of experimental conditions. Whereas small-gap load cells optimally designed for vacuum operation would perform poorly in air, large-gap designs allow 1–100 nN resolutions at atmospheric pressure, significantly expanding the range of applications of the proposed concept (albeit at a decrease in versatility, as air designs are range-independent only for thin devices). A sub-optimal prototype of the load cell was fabricated using (SOG) technology. A driving/sensing scheme was implemented and a resolution of ∼23 nN at a vacuum level of ∼50 mTorr (easily achievable with a mechanical pump) was demonstrated. The measured resolution (obtained with conventional packaging designs and testing conditions) was only an order of magnitude worse than predicted by the analytical model—consistently with the ubiquitous presence of unaccountable sources of noise. Given the exceptionally high resolutions revealed by the analytical/numerical optimization procedure, this result confirms (i) the robustness of the proposed model as an optimal design tool and (ii) the great potential of resonant load cells for unique combinations of force range and resolution. The development of PCB-mounted optimal driving/sensing circuits for maximum resolution and the details of the micro-load cell packaging and interfacing with external samples will be published in a future article. With unprecedented combination of force range, resolution, versatility, *in situ* optical (or SEM) access to the sample and low cost, the

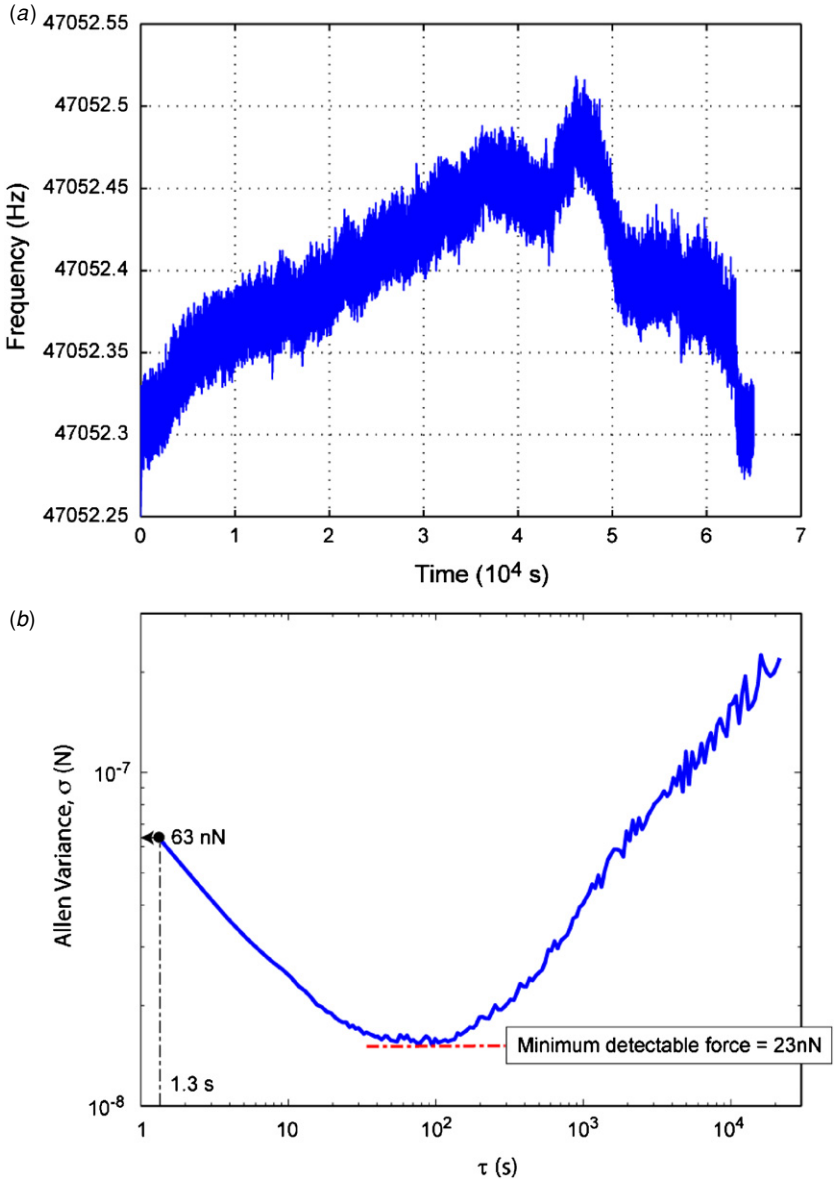


Figure 13. Noise analysis on the device depicted in figure 10. (*a*) Output drift of the micro-load cell, over a time scale of 18 h. (*b*) Allan variance analysis on the acquired data to investigate the most efficient signal integration time and extract the minimum detectable force (∼23 nN).

proposed micro-test frame will occupy a unique position in the rich world of micro and nano-mechanical testing tools.

Acknowledgments

This research was partly supported by the 2009 California-Catalonia Program for Engineering Innovation. AT and LV would like to thank Andrea Pantano for useful discussions and implementation of the optimization algorithm. KA and LV are thankful to Manuel Gamero-Castano for the use of his vacuum chamber. The authors wish to acknowledge the METU-MEMS Center staff at Middle East Technical University (who helped during the fabrication of the devices) and the Carl Zeiss Center for Excellence in Electron Microscopy at the University of California, Irvine.

Appendix A. Electro-mechanical model of a double-ended tuning fork

In the desired actuation mode, the vibration of the DETF is symmetric about its longitudinal axis, allowing modeling of an individual tine only. The geometric variables and reference system are depicted in figure 5. The dynamic response of the tine is governed by the equation of motion [21]:

$$\frac{\partial^2}{\partial x^2}\left(\mathrm{EI}\frac{\partial^2 v(x,t)}{\partial x^2}\right)+\frac{\partial}{\partial x}\left(\frac{F_{\mathrm{appl}}}{2}\frac{\partial v(x,t)}{\partial x}\right)+\rho A\frac{\partial^2 v(x,t)}{\partial t^2}=P_e(x,t), \tag{A.1}$$

where v is the deflection in the y direction, EI is the flexural stiffness of the tine for bending in the (x, y) plane, F_{appl} is the external axial force on the load cell (equal to twice the

force applied on each tine), ρ is the materials mass density, A is the cross-sectional area of the tine and P_e is the transverse actuation force. For the geometry depicted in figure 5, P_e is a concentrated force at the middle point of the tine (whereas it would be a distributed force along the tine length for driving without actuation plates). If the tine is forced with a combination of V_{dc} and V_{ac} at a frequency ω_n, as shown schematically in figure 10, the transverse electrostatic force is given by [16, 23]

$$P_e(t) = \frac{1}{2}\frac{\varepsilon_0 h L_p}{(g-y)^2}V^2(t) = \frac{1}{2}\frac{\varepsilon_0 h L_p}{(g-y)^2} \times \left[V_{dc}^2\frac{V_{ac}^2}{2} + 2V_{dc}V_{ac}\cos(\omega t) + V_{ac}^2\cos(2\omega t)\right] \quad (A.2)$$

with ε_0 the dielectric constant of vacuum ($\varepsilon_{air} \sim \varepsilon_0$), h the tine thickness in the z direction (i.e. the device structural thickness), L_p the length of the actuation plate and g the actuation plate capacitor gap. If ω is the DETF resonant frequency, then the higher frequency term is automatically filtered out. The linear term of the Taylor expansion in y acts as a negative stiffness term (electrostatic softening), namely $K_{electr} = -\varepsilon_0 h L_p (V_{dc}^2 + V_{ac}^2/2)/g^3$.

If we assume that a solution can be found by separation of variables, i.e. $v(x,t) = \phi(\varepsilon)y(t)$, with $\varepsilon = x/L$, the solution for the ith vibration mode can be written as [16]

$$\ddot{y}_i + \frac{\omega_n}{Q}\dot{y}_i + \omega_n^2 y_i = \frac{\varepsilon_0 h L_p}{M_{eff} g^2}V_{dc}V_{ac}\cos(\omega t), \quad (A.3)$$

where

$$K_{eff} = 2\frac{EI}{L^3}\int_0^{1/2}\left(\frac{d^2\phi_i}{d\varepsilon^2}\right)^2 d\varepsilon + 2\frac{F_{appl}/2}{L} \times \int_0^{1/2}\left(\frac{d\phi_i}{d\varepsilon}\right)^2 d\varepsilon - \frac{\varepsilon_0 h L_p}{g^3}\left(V_{dc}^2 + \frac{V_{ac}}{2}\right)$$

$$M_{eff} = 2\rho A L\int_0^{1/2}\phi_i^2\, d\varepsilon + \sum_j m_j(\phi_i(\varepsilon_j))^2 \quad (A.4)$$

$$\omega_n = \sqrt{\frac{K_{eff}}{M_{eff}}}$$

$$Q = \frac{M_{eff}\omega_n}{c}$$

with ϕ_i the vibration mode and m_j the mass of the actuation plate (modeled as a lumped mass). Equation (A.3) assumes that $y_i \ll g$. This condition will be imposed in the optimization study. The term $\omega_n\dot{y}/Q$ has been added to represent mechanical losses. Estimation of c (and hence Q) as a function of device geometry and ambient pressure is performed with existing analytical models [37–39], calibrated on experimental results. Approximating the mode shape to the elastic curve for a clamped–clamped beam subjected to a point load at its center, i.e. $\phi_i = \phi_1 = 16\varepsilon^3 - 12\varepsilon^2 + 1$, stiffness and mass can be evaluated as

$$K_{eff} = 192\frac{EI}{L_f^3} + 2.4\frac{F_{appl}}{L_f} - \frac{\varepsilon_0 h L_p}{g^3}\left(V_{dc}^2 + \frac{V_{ac}^2}{2}\right)$$

$$M_{eff} = \frac{13}{35}\rho\, h\, w_f L_f + \rho\, h\,(w_p L_p + w_c L_c). \quad (A.5)$$

The applied axial force has a linear effect on the effective stiffness. The sensitivity of the device (defined as the frequency change corresponding to a unit change in applied force) is

$$\frac{\partial\omega_n}{\partial F_{appl}} = \frac{1.2}{\omega_n M_{eff} L}. \quad (A.6)$$

The solution to equation (A.3) provides the tine displacement as [21]

$$y(t) = \frac{V_{dc}V_{ac}\varepsilon_0 h L_p/g^2}{K_{eff}\sqrt{\left(1-\left(\frac{\omega}{\omega_n}\right)^2\right)^2 + \left(\frac{\omega}{Q\omega_n}\right)^2}}\cos(\omega t + \varphi), \quad (A.7)$$

where the phase shift, φ, is given by

$$\varphi = \arctan\left(\frac{\omega/\omega_n}{Q(1-(\omega/\omega_n)^2)}\right). \quad (A.8)$$

If the device is driven at resonance ($\omega = \omega_n$) with the circuit depicted in figure 10, the output voltage is

$$V_{out}(t) = -R_{amp}V_{dc}\frac{\partial C}{\partial y}\dot{y}(t) \approx Q R_{amp}V_{dc}V_{ac}\left(\frac{\varepsilon_0 h L_p}{g^2}\right)^2\frac{\omega_n}{K_{eff}}\cos(\omega_n t), \quad (A.9)$$

where R_{amp} is the resistance of the trans-impedance amplifier.

Appendix B. Phase noise estimation

For conservativeness, we assume that the output signal V_{out} and the noise signal V_{noise} be in quadrature (worst case scenario). Hence the output voltage that is effectively measured is

$$V_{out}^{eff} = V_{out}\cos(\omega t + \varphi + \pi/2) + V_{noise}\cos(\omega t + \varphi) = \sqrt{V_{out}^2 + V_{noise}^2}\cos\left(\omega t + \varphi + \pi/2 + \arctan\left(\frac{V_{noise}}{V_{out}}\right)\right). \quad (B.1)$$

In other words, the noise at the output voltage V_{noise} induces a phase noise equal to

$$\Delta\varphi_{noise} = \arctan\left(\frac{V_{noise}}{V_{out}}\right). \quad (B.2)$$

Hence, at resonance:

$$\Delta\varphi_{noise} = \left.\frac{\partial\varphi}{\partial\omega}\right|_{\omega=\omega_n}\cdot\Delta\omega_{noise} = \frac{2Q}{\omega_n}\Delta\omega_{noise} \quad (B.3)$$

from which we finally estimate the minimum force that the load cell can resolve:

$$F_{min} = F_{noise} = \frac{\Delta\omega_{noise}}{\partial\omega/\partial F} = \frac{1}{\partial\omega/\partial F}\frac{\omega_n}{2Q}\arctan\left(\frac{V_{noise}}{V_{out}}\right). \quad (B.4)$$

Appendix C. Optimization algorithm

All optimizations were performed using a custom-built modified PSO governed by a spectral optimizer [33]. PSO are a class of optimizers that model a dynamic population system roaming through a problems parameter space searching for optimal function values [40]. Each member of the population, called a particle, maintains a record of the location where it has seen its best value on the function and also has visibility to the PSO's record of the population's best value and location as a whole. Each particle is attracted to its best local result as well as the PSO's best global result through equations of motion implemented discretely with simple forward Euler integration:

$$\begin{aligned} v_{n+1} &= w \cdot v_n + c_1 \cdot rand() \cdot (x_{\text{localbest},n} - x_n) \\ &\quad + c_2 \cdot rand() \cdot (x_{\text{globalbest},n} - x_n) \\ x_{n+1} &= x_n + \Delta t \cdot v_{n+1}, \end{aligned} \tag{C.1}$$

where *rand*() indicates a random number in the range [0, 1]. For the current analysis, we used: $w = 9, c_1 = c_2 = 2, \Delta t = 1$. Initial PSO optimization runs consisted of 1000 particles running for 100 iterations each at time step of 1.0. Particles were allowed to run until exhaustion, i.e. subsequent generations of 100 iterations were allowed to occur until no update to the global best result was recorded over the course of a generation.

As the force range for the load cell was discretized in 641 intervals and for each interval one PSO optimization run was performed (see section 3.2), a custom-built spectral optimizer was employed to ensure smoothness in figures 6–8, by reducing the noise and eliminating erratic results. The spectral optimizer was programmed for three follow-up operations to promote consistency in the results by providing 'reasonable' locations for the PSO to look for better results: (i) parameter values were fed forward to adjacent optimizations in the sequence with the PSO directed to densely populate a small hyper-cubic region of space surrounding those locations; (ii) parameter values were then fed backward under the same principle; (iii) noise detection was performed on the error of objective results and the parameter values relative to each optimizations neighbor in the sequences and further optimization prioritized based on the error level; PSO was directed to densely populate a hyper-rectangular region of parameter space bounded by the two adjacent results' best parameter values.

References

[1] Haque M A and Saif T 2008 Mechanical testing and the micro/nano scale *Springer Handbook of Experimental Solid Mechanics* ed W N Sharpe (New York: Springer)

[2] Bell D J, Lu T J, Fleck N A and Spearing S M 2005 MEMS actuators and sensors: observations on their performance and selection for purpose *J. Micromech. Microeng.* **15** S153–64

[3] Coleman J N, Khan U, Blau W J and Gun'ko Y K 2006 Small but strong: a review of the mechanical properties of carbon nanotube-polymer composites *Carbon* **44** 1624–52

[4] Greer J R and Nix W D 2006 Nanoscale gold pillars strengthened through dislocation starvation *Phys. Rev.* B **73** 245410

[5] Hollister S J 2005 Porous scaffold design for tissue engineering *Nature Mater.* **4** 518–24

[6] Zhang X, Jiang X N and Sun C 1999 Micro-stereolithography of polymeric and ceramic microstructures *Sensors Actuators* A **77** 149–56

[7] Jacobsen A J, Barvosa-Carter W and Nutt S 2007 Micro-scale truss structures formed from self-propagating photopolymer waveguides *Adv. Mater.* **19** 3892–6

[8] Greer J R, Jang D C, Kim J Y and Burek M J 2009 Emergence of new mechanical functionality in materials via size reduction *Adv. Funct. Mater.* **19** 2880–6

[9] Espinosa H D, Zhu Y and Moldovan N 2007 Design and operation of a MEMS-based material testing system for nanomechanical characterization *J. Microelectromech. Syst.* **16** 1219–31

[10] Haque M A and Saif M T A 2001 Microscale materials testing using MEMS actuators *J. Microelectromech. Syst.* **10** 146–52

[11] Kim K, Liu X, Zhang Y and Sun Y 2008 Nanonewton force-controlled manipulation of biological cells using a monolithic MEMS microgripper with two-axis force feedback *J. Micromech. Microeng.* **18** 055013

[12] Liu R, Wang H, Li X P, Ding G F and Yang C S 2008 A micro-tensile method for measuring mechanical properties of MEMS materials *J. Micromech. Microeng.* **18** 065002

[13] Tibrewala A, Phataralaoha A and Buttgenbach S 2008 Simulation, fabrication and characterization of a 3D piezoresistive force sensor *Sensors Actuators* A **147** 430–5

[14] Muntwyler S, Beyeler F and Nelson B J 2010 Three-axis micro-force sensor with sub-micro-Newton measurement uncertainty and tunable force range *J. Micromech. Microeng.* **20** 025011

[15] Fukuzawa K, Ando T, Shibamoto M, Mitsuya Y and Zhang H D 2006 Monolithically fabricated double-ended tuning-fork-based force sensor *J. Appl. Phys.* **99** 094901

[16] Roessig T A W 1998 Integrated MEMS tuning fork oscillators for sensor applications *Mechanical Engineering* (Berkeley, CA: University of California) p 137

[17] Seshia A A 2002 Integrated micromechanical resonant sensors for inertial measurement systems *Electrical Engineering and Computer Science* (Berkeley, CA: University of California)

[18] Lee J E Y, Bahreyni B and Seshia A A 2008 An axial strain modulated double-ended tuning fork electrometer *Sensors Actuators* A **148** 395–400

[19] Peng P, Rajamani R and Erdman A G 2009 Flexible tactile sensor for tissue elasticity measurements *J. Microelectromech. Syst.* **18** 1226–33

[20] Sokhanvar S, Packirisamy M and Dargahi J 2009 MEMS endoscopic tactile sensor: toward *in-situ* and *in-vivo* and tissue softness characterization *IEEE Sensors J.* **9** 1679–87

[21] Den Hartog J P 1985 *Mechanical Vibrations* (New York: Dover)

[22] Gabrielson T B 1993 Mechanical-thermal noise in micromachined acoustic and vibration sensors *IEEE Trans. Electron Devices* **40** 903–9

[23] Kaajakari V 2009 *Practical MEMS: Design of Microsystems, Accelerometers, Gyroscopes, RF MEMS, Optical MEMS, and Microfluidic Systems* (Las Vegas, NV: Small Gear Publishing)

[24] Andrews M, Harris I and Turner G 1993 A comparison of squeeze-film theory with measurements on a microstructure *Sensors Actuators* A **36** 79–87

[25] Blech J J 1983 On isothermal squeeze films *Trans. ASME J. Lubr. Technol.* **105** 615–20

[26] Collette Y 2003 *Multiobjective Optimization: Principles and Case Studies* (Berlin: Springer)

[27] Miller K, Cowen A, Hames G and Hardy B *SOIMUMPS Design Handbook* Available at http://www.memscap.com/en_mumps.html
[28] Gad-El-Hak M ed 2006 *MEMS: Introduction and Fundamentals* (Boca Raton, FL: CRC Press)
[29] Petersen K E 1982 Silicon as a mechanical material *Proc. IEEE* **70** 420–57
[30] Wortman J J and Evans R A 1965 Young's modulus, shear modulus, and Poisson's ratio in silicon and germanium *J. Appl. Phys.* **36** 153–6
[31] Hu S M 1982 Critical Stress in silicon brittle-fracture, and effect of ion-implantation and other surface treatments *J. Appl. Phys.* **53** 3576–80
[32] Johansson S, Ericson F and Schweitz J A 1989 Influence of surface-coatings on elasticity, residual-stresses, and fracture properties of silicon microelements *J. Appl. Phys.* **65** 122–8
[33] Godfrey S W 2010 Optimal design of orthotropic fiber-composite corrugated-core sandwich panels under axial compression *Mechanical and Aerospace Engineering* (Irvine, CA: University of California)
[34] Topalli E S, Topalli K, Alper S E, Serin T and Akin T 2009 Pirani vacuum gauges using silicon-on-glass and dissolved-wafer processes for the characterization of MEMS vacuum packaging *IEEE Sensors J.* **9** 263–70
[35] IEEE Std 1997 IEEE standard specification format guide and test procedure for single-axis interferometric fiber optic gyros IEEE Std 952
[36] Allan D W 1966 Statistic of atomic frequency standards *Proc. Inst. Electr. Electron. Eng.* **54** 221–30
[37] Cho Y H, Kwak B M, Pisano A P and Howe R T 1994 Slide film damping in laterally driven microstructres *Sensors Actuators* A **40** 31–9
[38] Lifshitz R and Roukes M L 2000 Thermoelastic damping in micro- and nanomechanical systems *Phys. Rev.* B **61** 5600–9
[39] Veijola T, Kuisma H, Lahdenpera J and Ryhanen T 1995 Equivalent-circuit model of the squeezed gas film in a silicon accelerometer *Sensors Actuators* A **48** 239–48
[40] Robinson J and Rahmat-Samii Y 2004 Particle swarm optimization in electromagnetics *IEEE Trans. Antennas Propag.* **52** 397–407